

# Impact strength of small icy bodies that experienced multiple collisions



Minami Yasui<sup>a,\*</sup>, Ryo Hayama<sup>b</sup>, Masahiko Arakawa<sup>b</sup>

<sup>a</sup> Organization of Advanced Science and Technology, Kobe University, 1-1, Rokkodai-cho, Nada-ku, Kobe 657-8501, Japan

<sup>b</sup> Graduate School of Science, Kobe University, 1-1, Rokkodai-cho, Nada-ku, Kobe 657-8501, Japan

## ARTICLE INFO

### Article history:

Received 6 November 2013

Revised 2 February 2014

Accepted 4 February 2014

Available online 20 February 2014

### Keywords:

Impact processes

Ices

Cratering

Kuiper belt

Satellites, surfaces

## ABSTRACT

Frequent collisions are common for small bodies in the Solar System, and the cumulative damage to these bodies is thought to significantly affect their evolution. It is important to study the effects of multiple impacts such as the number of impacts on the impact strength and the ejection velocity of impact fragments. Here we conducted multiple-impact experiments using a polycrystalline water ice target, varying the number of impacts from 1 to 10 times. An ice cylindrical projectile was impacted at 84–502 m s<sup>−1</sup> by using a single-stage gas gun in a cold room between −10 and −15 °C. The impact strength of the ice target that experienced a single impact and multiple impacts is expressed by the total energy density applied to the same target,  $\Sigma Q$ , and this value was observed to be 77.6 J kg<sup>−1</sup>. The number of fine impact fragments at a fragment mass normalized by an initial target mass,  $m/M_{t0} \sim 10^{-6}$ ,  $n_m$ , had a good correlation with the single energy density at each shot,  $Q_i$ , and the relationship was shown to be  $n_m = 10^{1.02 \pm 0.22} \cdot Q_i^{1.31 \pm 0.12}$ . We also estimated the cumulative damage of icy bodies as a total energy density accumulated by past impacts, according to the crater scaling laws proposed by Housen et al. (Housen, K.R., Schmidt, R.M., Holsapple, K.A. [1983]. J. Geophys. Res. 88, 2485–2499) of ice and the crater size distributions observed on Phoebe, a saturnian icy satellite. We found that the cumulative damage of Phoebe depended significantly on the impact speed of the impactor that formed the craters on Phoebe; and the cumulative damage was about one-third of the impact strength  $\Sigma Q^*$  at 500 m s<sup>−1</sup> whereas it was almost zero at 3.2 km s<sup>−1</sup>.

© 2014 Elsevier Inc. All rights reserved.

## 1. Introduction

In the evolution of Solar System bodies, collisional disruption has played an important role. For example, the proto-planets were formed by collisional disruption and the re-accumulation of planetesimals, and asteroids are believed to be survivors of planetesimals that experienced collisional disruption. In order to study the formation processes of Solar System bodies, the impact condition of catastrophic disruption for solid materials simulating various Solar System bodies should be clarified.

The impact condition for catastrophic disruption is called the impact strength,  $Q^*$ , and  $Q^*$  is one of the most important properties of Solar System bodies related to mutual impact.  $Q^*$  is defined by the energy density  $Q$  when the largest fragment mass is equal to one-half of the original target mass (Davis and Ryan, 1990), and the energy density  $Q$  is defined by the kinetic energy of the impactor (or projectile) divided by the original target mass. Over the past 30 years, many studies have been conducted to discern the impact strength of various solid materials simulating Solar System bodies,

such as laboratory impact experiments using basalt and ice (e.g., Fujiwara et al., 1977; Kawakami et al., 1983; Takagi et al., 1984; Davis and Ryan, 1990; Kato et al., 1995).

As spacecraft explorations and ground-based observations have advanced, more and more details of Solar System bodies have been revealed. For example, some asteroids and small icy satellites have low bulk density, i.e., large porosity (Consolmagno and Britt, 1998; Britt et al., 2002; Porco et al., 2007), and they are composed of a mixture of several components such as ices and silicates. Intensive studies to elucidate the effects of the porosity and the mixture on the impact strength have been conducted using various porous materials and mixtures (e.g., Arakawa and Tomizuka, 2004; Shimaki and Arakawa, 2012). These studies clarified that the porosity and the multiple components significantly affected the impact strength, increasing or decreasing them. We propose that it is very important to study the impact strength of various materials simulating Solar System bodies with a wider range of physical and chemical properties.

One of the most important and most interesting physical properties is “multiple impacts”. The term “multiple impacts” refers to when a Solar System body has experienced many impacts with other bodies. In this study, we focused on Solar System bodies that have experienced multiple impacts. These bodies experienced

\* Corresponding author. Fax: +81 78 803 6684.

E-mail address: [minami.yasui@pearl.kobe-u.ac.jp](mailto:minami.yasui@pearl.kobe-u.ac.jp) (M. Yasui).

multiple impacts are called as “pre-impacted bodies”. Laboratory experiments, exploratory observations, and numerical simulations have obtained some potential evidence of multiple impacts for small bodies such as asteroids, comets, and icy satellites. The many craters found on the small bodies are expected to be accompanied by many fractures under and around the craters, because laboratory impact cratering experiments in water ice and gypsum demonstrated that the impact craters were always surrounded by many cracks (Kato et al., 1995; Yasui et al., 2012). Veverka et al. (2000) found a large impact crater together with many grooves on the surface of Eros, and they suggested that the grooves may extend toward the interior as fractures. They speculated that the grooves might be formed simultaneously by the impact forming the crater. Michel et al. (2003) did numerical simulations of collisions of parent bodies to explore the properties of the Karin family (one of the large asteroid families), and the outcomes of the simulations showed that the Karin family members must be the products of collisions of a parent body that experienced impacts previously. In order to study the collisional evolutions of Solar System bodies, the impact strength of the bodies that experienced multiple impacts should be also clarified, because the pre-impacted bodies could have many fractures inside, so that their impact strength could be smaller than that of an intact body. It is thus important to know how the impact strength decreases with the number of impacts compared with the intact body.

Several experimental studies have investigated the effects of multiple impacts on the impact strength of small bodies by using target materials of glass and basalt simulating a tektite and an asteroid. Gault and Wedekind (1969) conducted impact experiments using spherical glass targets simulating a tektite at the impact velocity of  $7.55 \text{ km s}^{-1}$ , for 1, 4, 7, and 19 impacts on different impact surfaces. They examined the relationship between the largest fragment mass normalized by the original target mass,  $m_i/M_t$ , and the total energy density,  $\Sigma Q$ , where  $\Sigma Q$  was the sum of each projectile kinetic energy applied to the same target divided by the initial target mass. They found that the relationship was very similar to that obtained for single-impact experiments, irrespective of the number of impacts. Housen (2009) conducted impact experiments on cylindrical basalt targets at the impact velocity of  $0.73\text{--}1.97 \text{ km s}^{-1}$  and he studied a single impact and two impacts on the same and different impact surfaces. He reported almost the same result as that obtained by Gault and Wedekind (1969). Nakamura et al. (1994) also conducted impact experiments on a spherical basalt target at impact velocities of  $2.8\text{--}3.2 \text{ km s}^{-1}$  for a single impact and two impacts. We found that the result reported by Nakamura et al. was very different from that obtained by Housen (2009): the relationships between  $m_i/M_t$  and  $\Sigma Q$  in the two impacts was not consistent with that obtained by Housen (2009), whereas the relationship between  $m_i/M_t$  and the single energy density in the two impacts was almost similar to that obtained in single-impact experiments (Fujiwara and Tsukamoto, 1980; Takagi et al., 1984).

This difference could be caused by one or more target physical conditions such as the crack number density or distribution. Nakamura et al. (1994) used a barrel-shaped core fragment for the second shot, which was derived from an original target at the first shot. It was shown by a numerical simulation that the core fragment is not fractured so severely (Benz and Asphaug, 1993), and the pre-existing cracks inside the target given by the previous impacts in the target were fewer than that used by Housen (2009) in the second shot. Thus, in order to determine the precise effects of multiple impacts on the impact strength, the target physical conditions should be controlled. The crack number density and the distribution, in particular, should be systematically controlled.

In this study, we conducted multiple-impact experiments to study the effects of multiple impacts on the impact strength. We used a polycrystalline water ice target because there are no

experimental results for multiple impacts using an ice target, and water ice is a transparent material that is suitable for recognizing cracks in the target. In order to control the crack number density and the distribution in the targets, we systematically selected the number of impacts, the energy density at each impact shot (the single energy density:  $Q_j$ ), and the total energy density ( $\Sigma Q$ ). We also measured the ejecta velocity and the size distribution of impact fragments to characterize the degree of the impact disruption. Lastly, we attempted to apply our laboratory results for the estimation of the internal damage of a saturnian icy satellite, Phoebe, by using the crater scaling law proposed by Housen et al. (1983) and the cumulative size distributions of impact craters observed on the satellite.

## 2. Experimental methods

### 2.1. Samples

We used polycrystalline water ice as a projectile and as a target simulating icy bodies such as icy satellites and comets. The projectile was cylindrical (15-mm dia., height of 9–11 mm), with the mass,  $m_p$ , of 1.40–1.66 g. It was made by putting tap water put into a mold, and then freezing the water in a cold room ( $-10^\circ\text{C}$ ) for a few tens of minutes. The projectile looked cloudy because tiny bubbles were incorporated in it, and thus the projectile had a small amount of porosity (less than a few percent); however, the porosity did not affect the impact outcomes (Kato et al., 1995; Arakawa et al., 2002).

The target had a cubic shape with the initial mass ranging from 0.60 to 2.69 kg and the size from 8.7 to 14.0 cm. It was prepared by cutting a large commercial ice block. The density of the ice target was  $917 \text{ kg m}^{-3}$ , and the target was so-called “columnar ice” with large ice crystals elongated toward one direction with the size of several cm (Kato et al., 1995). There were no bubbles in it, so it looked completely transparent.

### 2.2. Impact experiments

We conducted impact experiments by using a one-stage light-gas gun installed in a cold room at the Institute of Low Temperature Science, Hokkaido University. A schematic illustration of the experimental setup is shown in Fig. 1. The impact velocity,  $V_i$ , ranged from 84 to  $502 \text{ m s}^{-1}$ . The room temperature was set between  $-10$  and  $-15^\circ\text{C}$ .

In the present study, an ice projectile was impacted on the same target from 1 to 10 times (=the number of impacts), and each impact was conducted on different target surfaces: the projectile was impacted on the intact surface up to four times, after that the surface that experienced the impact before was impacted again. A second shot was given to the opposing surface of the first shot, a third shot was given to the surface perpendicular to those of the first and second shots, and a fourth shot was given to the opposing surface of the third shot, and so on. We used these four surfaces to give the impact on the target, and then these surfaces were impacted two to three times repeatedly in one series of experiment for fifth to tenth shots. The other two intact surfaces were used for a window to observe the generated cracks inside the target.

In the present study, we describe the target mass according to the number of impacts: (1) the target mass before the first impact,  $M_{t0}$  (initial target mass), and (2) the target mass before the  $j$ th impact ( $j = 2\text{--}10$ ),  $M_{t,j}$ . We describe the impact condition by using two parameters: (1) the energy density at each shot or a single energy density,  $Q_j$ , where the subscript  $j$  is the number of impacts, and (2) the total energy density,  $\Sigma Q$ , which corresponds to the sum of each energy density applied to the same target, that is,

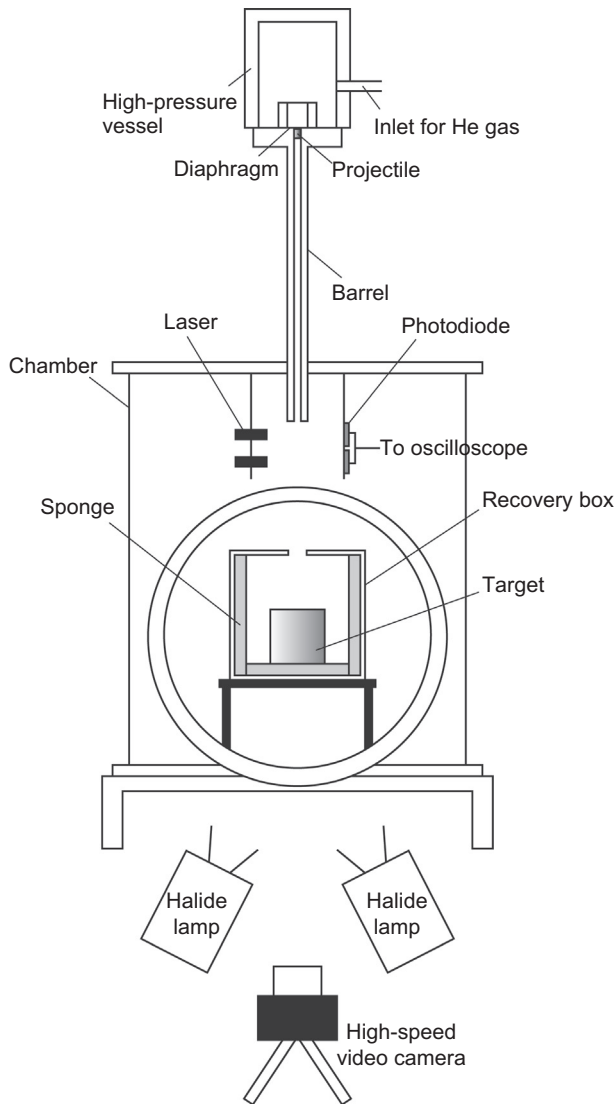


Fig. 1. Schematic of the experimental apparatus of the single-stage gas gun.

the  $\Sigma Q$  is equal to  $\sum_{j=1}^n Q_j$  ( $j = 1-10$ ). The single energy density  $Q_j$  is written as  $Q_j = \frac{1}{2} m_p V_i^2 / (m_p + M_{t,j})$  where  $M_{t,j}$  is the target mass before the  $j$ th impact. At  $j = 1$ ,  $Q_1$  is written as  $Q_1 = \frac{1}{2} m_p V_i^2 / (m_p + M_{t0})$ .

As illustrated in Fig. 1, the target was placed at the bottom of a recovery box so that we could collect the impact fragments after the shot, and the box was covered with sponge plates on the bottom and three sides to prevent these fragments from secondary collisions against the walls of the box. The uncovered side was used for the window to observe the impact phenomena, from which we measured the ejecta velocity, particularly that ejected from the corner points on the impact surface. The recovery box was set in a sample chamber, and the impact experiment was conducted under air pressure during the shots at impact velocities lower than  $340 \text{ m s}^{-1}$ . At impact velocities higher than  $340 \text{ m s}^{-1}$ , the chamber was evacuated below  $10^4 \text{ Pa}$  to avoid loud noise generation in air. After the shot, we measured the mass of each recovered fragment one by one with an electric mass balance for the fragments larger than  $0.01 \text{ g}$ . The residual fragments smaller than  $0.01 \text{ g}$  were sieved into seven groups of size range, and we measured the total mass of fragments at each size range.

We observed the collisional disruption of the target using a high-speed digital video camera to measure the ejecta velocity.

The frame rate was set from  $4.0 \times 10^3$  to  $1.0 \times 10^4 \text{ frames s}^{-1}$ , and the shutter speed was set from 10 to  $50 \mu\text{s}$ . We observed the collisional disruption process by illuminating the target using two metal halide lamps from the front of the target.

The fluctuation of the room temperature did not affect the experimental results in this study. This temperature range is higher than the average temperature of the outer Solar System where icy satellites exist (below 100 K). Kato et al. (1992) did impact experiments using polycrystalline water ice at 77 and 255 K, and they found that the energy density,  $Q$ , required to disrupt the 77-K ice target to about 1/20 of the original target mass was five times larger than that required for the 255-K ice target. We therefore felt that the effect of multiple impacts on the impact strength of polycrystalline water ice at lower temperatures should be examined, and we are planning to conduct such a study.

### 3. Results

The experimental condition of each shot is summarized in Table 1. In this study, we made a series of multiple-impact experiments with 32 targets, and then 92 shots in total were conducted. We changed both the energy density for each shot,  $Q_j$ , and the total energy density,  $\Sigma Q$ , and the series was classified into three groups. The first group was the series with an equal energy density for every shot on the same target. The second group was the series with a final energy density,  $Q_f$ , larger than the impact strength of polycrystalline ice,  $Q_{ice}^* = 71.5 \text{ J kg}^{-1}$  (Kato et al., 1995). The third group was the series of different energy densities for every shot on the same target, but not satisfying the condition of the second group, that is,  $Q_f < Q_{ice}^*$ . This classification is shown in Table 1 as  $Q_j \sim \text{const}$ ,  $Q_f > Q_{ice}^*$ , and  $Q_j \neq \text{const}$ , respectively.

#### 3.1. Observation of collisional disruption

Fig. 2a–c are snapshots taken by the high-speed video camera during the disruption. All figures were taken for the shot at the same total energy densities,  $\Sigma Q$ , approx.  $100 \text{ J kg}^{-1}$ , however, the total numbers of impacts are different. The energy densities for one target given at every shot were almost the same; i.e.,  $Q_j$  is a constant ( $Q_j \sim \text{const}$ ). Fig. 2a shows the snapshots of the catastrophic disruption by a single impact, and the impact velocity was  $387 \text{ m s}^{-1}$ . The movie recorded during the collisional disruption is shown as Supplementary video S1 as Supplementary online material. The projectile impacted on the center of the top surface (the first image in Fig. 2a). After the projectile was impacted, many cracks were generated around the upper half region of the target (second image from the top), and then many small fragments were ejected outward from the impact points (third image from the top). After 30 ms, the target was largely deformed and looked to be disrupted catastrophically, and many fragments were scattered in the recovery box in the bottom image.

Fig. 2b and c are snapshots of the target damaged by multiple impacts; a double impact for Fig. 2b and a four-times impact for Fig. 2c. The final shots with the impact velocity of  $235 \text{ m s}^{-1}$  and  $181 \text{ m s}^{-1}$ , respectively are shown in Fig. 2b and c. The movies recorded during the collisional disruption for the double impact and the four-times impact are provided as Supplementary videos S2 and S3, respectively. In both cases, a few small impact fragments were observed to be ejected from their impact points at 10 ms (second images from the top of Fig. 2b and c). The targets were then split vertically and divided into two separate parts, and the V-shaped vertical gap is shown in the third images from the top of Fig. 2b and c.

Most of the fragments looked to be generated according to the pre-existing cracks which were formed by the previous shots: the pre-existing cracks were slightly disconnected from each other,

**Table 1**  
Impact conditions and results of all shots.

Number of impacts	Run number	Shot number	$V_i$ (m s <sup>-1</sup> )	$m_p$ (g)	$M_{i0}$ or $M_{LJ}$ (g)	$Q_j$ (J kg <sup>-1</sup> )	$\Sigma Q$ (J kg <sup>-1</sup> )	$m_i$ (g)	$V_{e-g}$ (m s <sup>-1</sup> )		$Q_j$ series
									Left	Right	
1	20121123-4	1	253	1.60	1089.0	47.06	47.06	1064.6	–	–	–
	20121123-5	1	254	1.60	1020.0	50.44	50.44	761.3	–	1.81 ( $1.39 \times 10^{-1}$ )	–
	20120221-5	1	256	1.50	764.9	64.26	64.26	559.8	–	–	–
	20110930-6*	1	387	1.60	1160.9	103.21	103.21	168.6	2.89 ( $9.37 \times 10^{-2}$ )	–	–
	20130911-1	1	395	1.58	803.4	153.62	153.62	85.5	4.06 ( $9.14 \times 10^{-2}$ )	4.44 ( $1.06 \times 10^{-1}$ )	–
	20110707-1	1	482	1.54	1014.4	176.35	176.35	60.4	8.28 ( $3.14 \times 10^{-1}$ )	7.97 ( $1.71 \times 10^{-1}$ )	–
	20130911-2	1	448	1.59	793.4	200.89	200.89	38.6	7.34 ( $9.54 \times 10^{-2}$ )	8.10 ( $1.14 \times 10^{-1}$ )	–
	20130914-3	1	502	1.57	595.5	332.00	332.00	30.4	13.39 ( $5.80 \times 10^{-1}$ )	11.13 ( $1.11 \times 10^{-1}$ )	–
2	20120221-1	1	266	1.40	1395.0	35.51	35.51	1383.4	–	–	$Q_j \sim \text{const}$
	20120225-2	2	215	1.61	1380.7	26.95	62.46	1371.3	–	–	–
	20130914-1	1	244	1.59	1030.6	45.97	45.97	1018.0	–	–	$Q_j \sim \text{const}$
	20130914-2	2	237	1.58	1018.0	43.67	89.64	554.6	–	–	–
	20130912-9	1	236	1.56	808.9	53.92	53.92	759.4	–	–	$Q_j \sim \text{const}$
	20130912-10*	2	235	1.57	759.4	56.93	110.85	135.4	0.95 ( $3.78 \times 10^{-2}$ )	1.44 ( $6.47 \times 10^{-2}$ )	–
	20130912-1	1	285	1.60	1051.6	61.57	61.57	835.4	1.78 ( $5.47 \times 10^{-2}$ )	2.47 ( $1.36 \times 10^{-1}$ )	$Q_j \sim \text{const}$
	20130912-2	2	280	1.57	835.4	73.87	135.44	80.9	2.37 ( $6.72 \times 10^{-2}$ )	2.65 ( $6.08 \times 10^{-2}$ )	–
	20120222-6	1	263	1.60	747.4	74.03	74.03	625.5	–	–	$Q_j \sim \text{const}$
	20120222-7	2	256	1.61	625.5	84.35	158.38	39.9	–	–	–
	20130913-5	1	234	1.57	596.1	71.90	71.90	513.2	–	–	$Q_j \sim \text{const}$
	20130913-6	2	236	1.60	513.2	86.81	158.71	55.7	2.39 ( $7.13 \times 10^{-2}$ )	2.98 ( $5.36 \times 10^{-2}$ )	–
	20110929-5	1	180	1.58	996.1	25.70	25.70	994.6	–	–	$Q_f \neq \text{const}$
	20111001-1	2	246	1.58	994.6	48.07	73.76	559.9	–	–	–
	20110929-4	1	184	1.58	1270.3	21.06	21.06	1269.6	–	–	$Q_f > Q_{ice}^*$
	20110930-5	2	383	1.59	1269.6	91.85	112.91	68.6	6.99 ( $1.15 \times 10^{-1}$ )	–	–
	20120220-1	1	140	1.57	1330.8	11.56	11.56	1329.6	–	–	$Q_f > Q_{ice}^*$
	20120225-3	2	408	1.57	1324.2	98.68	110.24	109.2	5.91 ( $2.81 \times 10^{-2}$ )	–	–
	20110929-1	1	254	1.60	1014.9	50.85	50.85	994.2	–	–	$Q_f > Q_{ice}^*$
	20110930-1	2	385	1.58	994.2	117.78	168.64	43.6	2.95 ( $1.23 \times 10^{-1}$ )	5.16 ( $1.73 \times 10^{-1}$ )	–
3	20130912-6	1	231	1.63	1535.3	28.43	28.43	1530.6	–	–	$Q_j \sim \text{const}$
	20130912-7	2	227	1.58	1530.6	26.71	55.14	1525.1	–	–	–
	20130912-8	3	231	1.56	1525.1	27.33	82.47	1084.0	–	–	–
	20121122-1	1	188	1.60	1005.6	28.09	28.09	1002.7	–	–	$Q_j \sim \text{const}$
	20121122-2	2	188	1.60	1002.2	28.06	56.15	1000.2	–	–	–
	20121122-3	3	193	1.60	999.1	29.83	85.98	590.7	0.47 ( $2.90 \times 10^{-2}$ )	0.80 ( $1.62 \times 10^{-1}$ )	–
	20121121-1	1	189	1.60	989.7	28.87	28.87	986.8	–	–	$Q_j \sim \text{const}$
	20121121-2	2	185	1.60	985.6	27.78	56.65	981.2	–	–	–
	20121121-3	3	192	1.60	980.6	30.07	86.73	971.0	–	–	–
	20130912-3	1	198	1.56	801.7	38.03	38.03	800.4	–	–	$Q_j \sim \text{const}$
	20130912-4	2	197	1.62	800.4	39.39	77.41	796.5	–	–	–
	20130912-5	3	200	1.66	796.5	41.65	119.06	485.6	1.37 ( $1.05 \times 10^{-1}$ )	1.75 ( $1.27 \times 10^{-1}$ )	–
	20110709-1	1	259	1.60	999.3	53.71	53.71	986.6	–	–	$Q_f > Q_{ice}^*$
	20110709-2	2	252	1.60	986.1	51.52	105.22	257.0	–	–	–
	20110709-3	3	250	1.60	241.6	206.96	312.19	12.7	4.86 ( $1.59 \times 10^{-1}$ )	3.61 ( $1.14 \times 10^{-1}$ )	–
4	20130913-1	1	171	1.59	1254.4	18.48	18.48	1251.6	–	–	$Q_j \sim \text{const}$
	20130913-2	2	192	1.56	1251.6	23.07	41.55	1249.8	–	–	–
	20130913-3	3	197	1.57	1249.8	24.35	65.90	1242.6	–	–	–
	20130913-4	4	196	1.57	1242.6	24.25	90.15	462.7	–	–	–
	20110708-2	1	186	1.60	1007.9	27.46	27.46	1006.1	–	–	$Q_j \sim \text{const}$
	20110708-3	2	186	1.60	1006.3	27.50	54.96	1004.9	–	–	–
	20110708-4	3	184	1.60	1003.6	26.99	81.95	967.1	–	–	–
	20110708-5*	4	181	1.60	967.1	27.10	109.05	120.8	0.66 ( $6.52 \times 10^{-2}$ )	0.70 ( $3.31 \times 10^{-2}$ )	–
	20110929-6	1	185	1.58	1173.1	23.05	23.05	1160.6	–	–	$Q_j \neq \text{const}$

	20111001-5	2	132	1.60	1160.6	12.01	35.06	1162.3	–	–	
	20111001-6	3	137	1.62	1162.7	13.08	48.14	1159.9	–	–	
	20111001-7	4	186	1.58	1159.9	23.56	71.70	1062.5	1.21 ( $2.69 \times 10^{-2}$ )	–	
	20110929-2	1	254	1.60	1143.2	45.15	45.15	1151.6	–	–	$Q_j \neq \text{const}$
	20110930-2	2	160	1.60	1151.6	17.78	62.93	1150.3	–	–	
	20110930-3	3	186	1.58	1150.3	23.76	86.69	1143.0	–	–	
	20110930-4	4	186	1.60	1143.0	24.21	110.91	521.6	0.60 ( $3.26 \times 10^{-2}$ )	–	
	20110929-3	1	247	1.60	1170.3	41.70	41.70	1162.0	–	–	$Q_j \neq \text{const}$
	20111001-2	2	140	1.60	1162.0	13.49	55.20	1161.3	–	–	
	20111001-3	3	138	1.57	1161.3	12.87	68.07	1159.3	–	–	
	20111001-4	4	194	1.60	1159.3	25.97	94.04	928.5	1.61 ( $5.90 \times 10^{-2}$ )	1.99 ( $2.94 \times 10^{-2}$ )	
	20120224-4	1	142	1.56	985.5	15.96	15.96	983.9	–	–	$Q_f > Q_{ice}^*$
	20120224-5	2	147	1.60	983.9	17.57	33.53	983.4	–	–	
	20120224-6	3	138	1.62	983.4	15.69	49.22	983.5	–	–	
	20120224-7	4	464	1.64	983.5	179.50	228.72	36.3	5.95 ( $2.09 \times 10^{-2}$ )	–	
7	20120221-2	1	141	1.60	1447.6	10.99	10.99	1437.5	–	–	$Q_j \sim \text{const}$
	20120221-3	2	140	1.59	1437.5	10.84	21.83	1432.9	–	–	
	20120221-4	3	124	1.60	1432.9	8.58	30.41	1432.0	–	–	
	20120225-1	4	143	1.57	1427.0	11.25	41.66	1425.1	–	–	
	20120225-4	5	141	1.60	1424.2	11.17	52.83	1420.6	–	–	
	20120225-5	6	146	1.59	1420.6	11.93	64.76	1410.5	–	–	
	20120225-6	7	142	1.58	1410.5	11.29	76.05	738.2	–	–	
8	20130913-7	1	132	1.58	800.1	17.22	17.22	799.6	–	–	$Q_j \neq \text{const}$
	20130913-8	2	112	1.58	799.6	12.34	29.56	799.5	–	–	
	20130913-9	3	128	1.59	799.5	16.32	45.88	798.2	–	–	
	20130913-10	4	111	1.59	798.2	12.30	58.19	796.0	–	–	
	20130913-11	5	115	1.58	796.0	13.09	71.27	681.1	–	–	
	20130913-12	6	84	1.57	681.1	8.12	79.40	679.3	–	–	
	20130913-13	7	148	1.58	679.3	25.33	104.72	588.7	–	0.57 ( $2.83 \times 10^{-2}$ )	
	20130913-14	8	126	1.56	588.7	20.93	125.65	182.9	–	0.66 ( $1.85 \times 10^{-2}$ )	
10	20120223-1	1	143	1.61	2689.0	6.12	6.12	2689.0	–	–	$Q_j \sim \text{const}$
	20120223-2	2	123	1.58	2688.1	4.45	10.57	2686.8	–	–	
	20120223-3	3	140	1.62	2686.8	5.91	16.48	2684.8	–	–	
	20120223-4	4	124	1.59	2682.2	4.56	21.03	2681.1	–	–	
	20120223-5	5	143	1.57	2679.2	5.99	27.03	2676.5	–	–	
	20120223-6	6	140	1.58	2676.3	5.79	32.81	2672.3	–	–	
	20120223-7	7	145	1.65	2671.3	6.49	39.30	2669.5	–	–	
	20120224-1	8	103	1.57	2637.4	3.16	42.46	2636.5	–	–	
	20120224-2	9	149	1.61	2635.1	6.78	49.24	2632.9	–	–	
	20120224-3	10	144	1.60	2632.9	6.30	55.55	977.5	–	–	

Number of impacts: The total numbers of projectiles impacted on the same target.

Run number: Asterisk (\*) indicates the results shown in Figs. 2, 4 and 5.

Shot number: The  $j$ th impact for a series of impact experiments on the same target.

$V_i$ : Impact velocity.

$m_p$ : Projectile mass.

$M_{i0}$  or  $M_{t,j}$ :  $M_{i0}$  is the initial target mass, and  $M_{t,j}$  is the target mass before the  $j$ th impact ( $j = 2-10$ ).

$Q_j$ : Energy density at the  $j$ th impact.

$\Sigma Q$ : Total energy density, which is the sum of each energy density applied to the same target obtained from first to  $j$ th shots.

$m_i$ : Largest impact fragment mass at the  $j$ th impact.

$V_{e-g}$ : The fragment velocities at two corners on the impact surface. The “left” is the velocity at the left corner of the target, and the “right” is the velocity at the right corner. The numbers in parentheses indicate the error.

$Q_j$  series: The classification of energy density obtained at each shot on the same target for a series of impact experiments. It is described in detail in the beginning of Section 3.



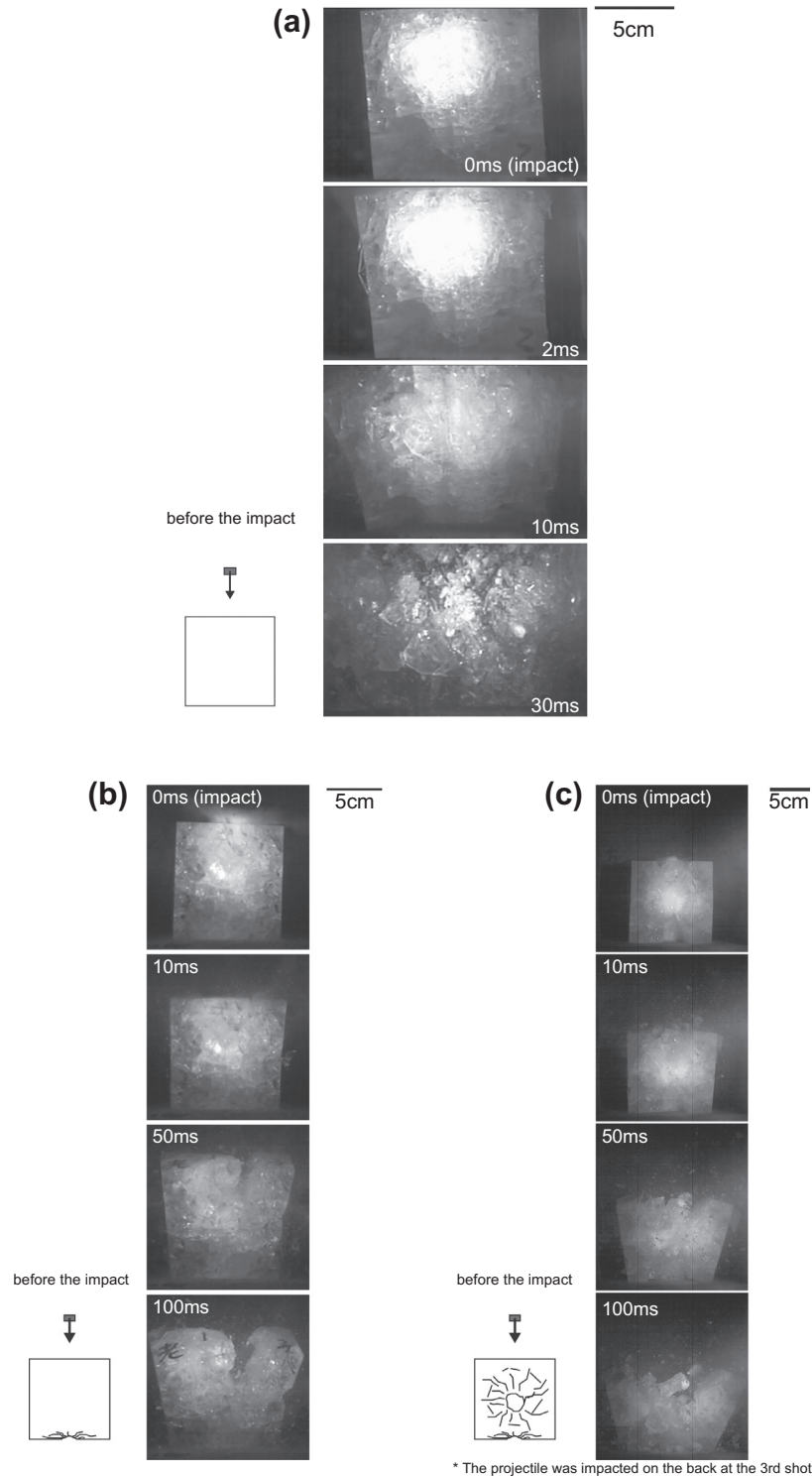


**Fig. 2.** Snapshots taken by the high-speed digital video camera. The number in each shot represents the elapsed time after the impact in ms. An elapsed time of 0 ms means the moment of impact. The scale is shown in each panel. The run numbers and the number of impacts were (a) 20110930-6, a single impact, (b) 20130912-10, a double impact, and (c) 20110708-5, a four-times impact. All panels show the  $Q_j$  series of  $Q_j \sim \text{const}$ , and they used the same total energy density  $\Sigma Q$  of approx.  $100 \text{ J kg}^{-1}$ . The schematic illustration on each panel at the bottom left shows the appearance of the projectile and target before the impact. The frame rates were 4000 fps in panel (a) and 5000 fps in panels (b) and (c).

and these cracks might be activated to grow slightly and connect to each other to form new fragments on the final shots. As shown in Fig. 2b and c, several large fragments at these corners were detached and had fallen over on the base of the recovery box from the initial positions shown in the bottom images of Fig. 2b and c. Thus, we observed that these fragments were ejected slowly compared to those of the single-impact experiments shown in Fig. 2a.

### 3.2. Fragment velocities

We measured the fragment velocities at two corners on the impact surface because these fragment velocities could be recognized as a representative of high-velocity fragments generated in a moderate disruption (Housen, 2009; Yasui and Arakawa, 2011). Fig. 3 shows the relationship between the  $V_{e-g}$  and the energy density

at each shot,  $Q_j$ , where  $V_{e-g}$  is the fragment velocity ejected from two corners on the impact surface in the center of the mass system. The velocity of the center of the mass system,  $V_g$ , is calculated by  $V_g = m_p V_i / (m_p + M_{t,j} \text{ or } m_p + M_{t0})$ . The detailed method to derive  $V_{e-g}$  is described in Yasui and Arakawa (2011).

We were able to measure two values of  $V_{e-g}$  on one target, so the average value for each target is plotted in Fig. 3, and the error bar indicates the range of the two  $V_{e-g}$  values at the left and right corners. We could measure the  $V_{e-g}$  at only one corner for some targets because of the haze covering the optical window. The  $V_{e-g}$  increased with the increase of energy density  $Q_j$ , irrespective of the number of impacts and the impact history for each target. All of the data can be fitted by one empirical equation as follows:

$$V_{e-g} = 10^{-1.53 \pm 0.18} \cdot Q_j^{1.03 \pm 0.09}, \quad (1)$$

for ice-on-ice impacts at the impact velocity  $V_i$  smaller than  $500 \text{ m s}^{-1}$  and the ratio of projectile to initial target,  $m_p/M_{t0}$ , from  $1.3 \times 10^{-3}$  to  $2.7 \times 10^{-3}$ .

### 3.3. Size distribution of recovered fragments

Fig. 4a–c are photographs of the recovered fragments from the different series of impact experiments with the same total energy density of  $100 \text{ J kg}^{-1}$ , but with different numbers of impacts: a single impact for Fig. 4a, a double impact for Fig. 4b, and a four-times impact for Fig. 4c. They are the same runs as those shown in Fig. 2. We found that the mass of the largest fragment in these figures was almost the same, irrespective of the number of impacts. On the other hand, the amount of fine fragments depended on the number of impacts: it was smaller for the multiple-impact experiments. Fig. 5 shows the size distribution of the recovered fragments in Fig. 4: the relationships between the cumulative number of fragments and the fragment mass normalized by the initial target mass,  $m_i/M_{t0}$ , are shown, so that the largest fragment mass corresponds to that at the cumulative number of unity. We were able to recover the impact fragments of >95% of the initial target for all shots. These distributions are almost similar until the normalized fragment mass was greater than approx.  $3.0 \times 10^{-4}$ , but they are clearly different at the normalized

fragment mass smaller than approx.  $3.0 \times 10^{-4}$ : the cumulative number of fine fragments is smaller for the multiple impacts even if the total energy density is the same.

In the following sections we describe the characteristics of the largest fragment mass and the fine fragments separately, because the effects of total energy density  $\Sigma Q$  and the single energy density  $Q_j$  on the catastrophic disruption are thought to be different: the  $\Sigma Q$  is an important parameter to determine the largest fragment mass, and the  $Q_j$  is related to the amount of fine fragments. We therefore discuss the effects of  $\Sigma Q$  on these fragments in the conditions classified based on the  $Q_j$  as follows:  $Q_j \sim \text{const}$ ,  $Q_f > Q_{ice}^*$ , and  $Q_j \neq \text{const}$ . It is well known that the largest fragment mass represents the degree of impact fragmentation, and it is usually used to determine the impact strength. Thus we first attempted to determine the impact strength of pre-impacted targets according to the largest fragment mass.

#### 3.3.1. Impact condition for the onset of collisional fragmentation and impact strength

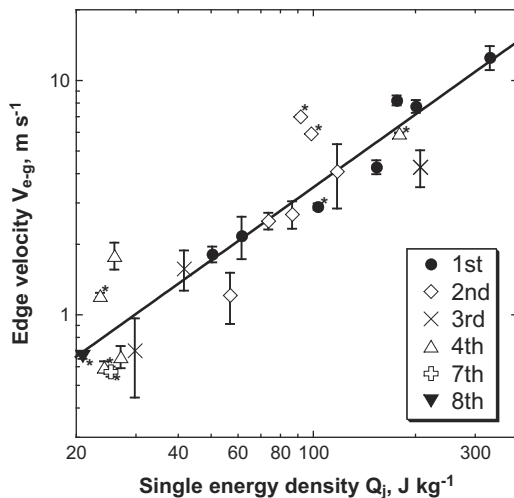
We showed in Fig. 5 that the largest fragment mass normalized by the initial target mass was almost the same when the total energy density,  $\Sigma Q$ , was close. We therefore studied the impact condition for the onset of collisional fragmentation, and we determine the impact strength of pre-impacted targets, which was usually derived from the relationship between the energy density and the largest fragment mass.

Fig. 6 shows the relationship between the  $\Sigma Q$  and the kinetic energy of the projectile for each shot. In this figure, the impact outcomes are divided into two groups: one group shows the normalized largest fragment mass larger than 0.95 and the other group shows that smaller than 0.95. The former group is classified as crater formation, and the latter group is classified as impact fragmentation. As shown in Fig. 6, the boundary between the area of crater formation and that of impact fragmentation was determined by a constant  $\Sigma Q$  value. This value was independent on the number of impacts and the series of impacts, although the boundary had a range of some width to show that both types appear at the  $\Sigma Q$  from  $50.4 \text{ J kg}^{-1}$  to  $86.7 \text{ J kg}^{-1}$ . It is very reasonable that the pre-impacted target was easily fractured by a small single energy density because of the pre-existing cracks inside the target given by the previous impacts. However, our results revealed an essential property of the pre-impacted target, that is, the onset of impact fragmentation for the pre-impacted target is always described by only one parameter of the constant total energy density,  $\Sigma Q_{\text{onset}}$ , irrespective of the impact history of each target. This means that a pre-impacted target that already received  $\Sigma Q_j$  by  $j$ -times impact will be disrupted by giving a single energy density  $Q_{j+1}$  at  $j+1$  times impact, which is equal to  $\Sigma Q_{\text{onset}} - \Sigma Q_j$ . The  $\Sigma Q_{\text{onset}}$  corresponding to this boundary was found to be  $68.6 \pm 18.2 \text{ J kg}^{-1}$ .

Fig. 7 shows the relationship between the single energy density  $Q_j$  and the largest fragment mass normalized by the initial target mass,  $m_i/M_{t0}$ , that is, when the same target was impacted at  $j$  times. The  $m_i/M_{t0}$  for each shot from the first to the  $j$ th shot was plotted in this figure. Each symbol indicates the turn of each impact. We found that the  $m_i/M_{t0}$  decreased with the increase of the number of impacts at the constant single energy density  $Q_j$ . Our single-impact (1st) data agreed well with those of the polycrystalline ice obtained in the single-impact experiments by Kato et al. (1995).

The impact strength  $Q^*$  is defined as the  $Q_j$  when the largest fragment mass is one-half of the original target mass, and thus we obtained the  $Q^*$  for each number of impacts from the single impact (1st) to the four-times impact (4th), respectively. We used the following equation to fit the data:

$$m_i/M_{t0} = 10^A \cdot Q_j^{-p}, \quad (2)$$



**Fig. 3.** The relationship between the fragment velocity at two corners on the impact surface in the center of the mass system,  $V_{e-g}$ , and the single energy density  $Q_j$ . The average values of the  $V_{e-g}$  measured at the left corner and at the right corner for each target are shown as a symbol. Error bar: the range of two  $V_{e-g}$  values. The solid line represents the fitting line determined using the power law function of Eq. (1). The asterisk \* at the upper or lower right corners of the symbol means the  $V_{e-g}$  at only one side corner on the target because of a fuzzy image.

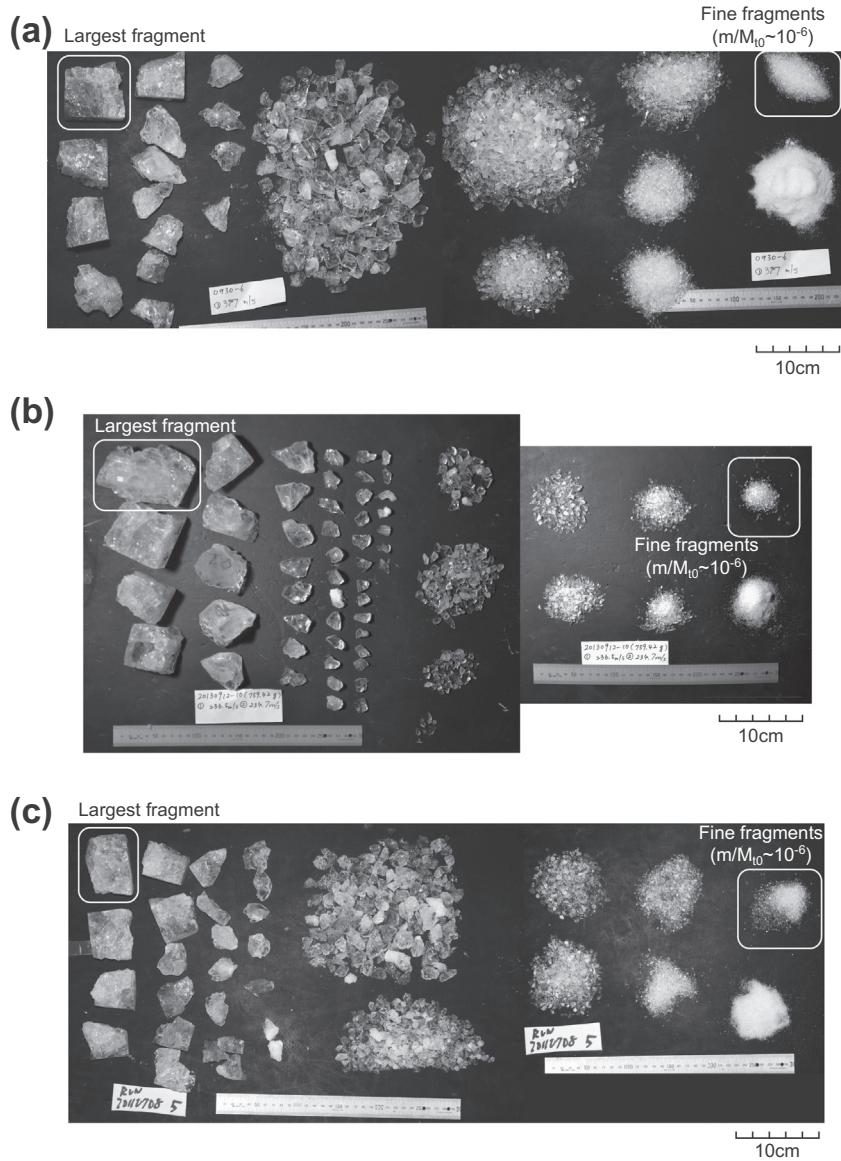


**Fig. 4.** Photographs of the recovered samples for the same targets as those shown in Fig. 2. (a) 20110930-6, a single impact, (b) 20130912-10, a double impact, and (c) 20110708-5, a four-times impact.

where  $A$  and  $p$  are constants, depending on the number of impacts. The parameters of  $A$  and  $p$ , and the impact strength  $Q^*$  for  $j$ th impacts ( $j = 1-4$ ) are shown in Table 2, and the relationship between the number of impacts and the  $Q^*$  are shown in Fig. 8. The data for the three-times impact (3rd) and the four-times impact (4th) were not enough to obtain the constants of Eq. (2). Thus, we assumed that the  $p$  for the three-times impact (3rd) and the four-times impact (4th) was the same as that for the double impact (2nd).

From Table 2, it can be seen that the parameters of our data and those of Kato et al. (1995) for single impacts are almost consistent with each other in the error range. We found that the impact strength  $Q^*$  decreased with the number of impacts  $j$ , and the empirical equation fitted by a power law equation could be obtained as  $Q^* = 10^{1.86 \pm 0.04j - 0.66 \pm 0.09}$ . Then, we consider the relationship between the  $m_i/M_{t0}$  and the total energy density,  $\Sigma Q$ , in the next paragraph.

Fig. 9 shows the relationship between the  $\Sigma Q$  and the  $m_i/M_{t0}$  for each series of impact experiments. The data were slightly scattered but they were almost all well approximated by one line. These

results agreed very well with the results of the single-impact experiments conducted by Kato et al. (1995). Thus, we can conclude that the  $m_i/M_{t0}$  was determined by the  $\Sigma Q$ , irrespective of the impact history for each target and the magnitude of each single energy density given to the same target. We can determine the empirical equation representing the relationship between the  $m_i/M_{t0}$  and the  $\Sigma Q$  for our results (not including the results of Kato et al. (1995)) at the  $m_i/M_{t0}$  smaller than 0.95 as follows:

$$\frac{m_i}{M_{t0}} = 10^{4.05 \pm 0.46} \cdot \Sigma Q^{-2.30 \pm 0.22}. \quad (3)$$

Compared with the  $A$  and the  $p$  of Eq. (2) for the results of Kato et al. (1995), it is clear that our results of Eq. (3) agree well with those of Kato et al. (1995) in the error range. Here, according to the definition of impact strength  $Q^*$  as mentioned above, we expanded the definition of the impact strength to the multiple impacts,  $\Sigma Q^*$ , which can be obtained from the relationship between  $m_i/M_{t0}$  and  $\Sigma Q$  for  $m_i/M_{t0} = 0.5$ . Then, the  $\Sigma Q^*$  is determined as  $77.6 \text{ J kg}^{-1}$ , irrespective of the number of impacts.



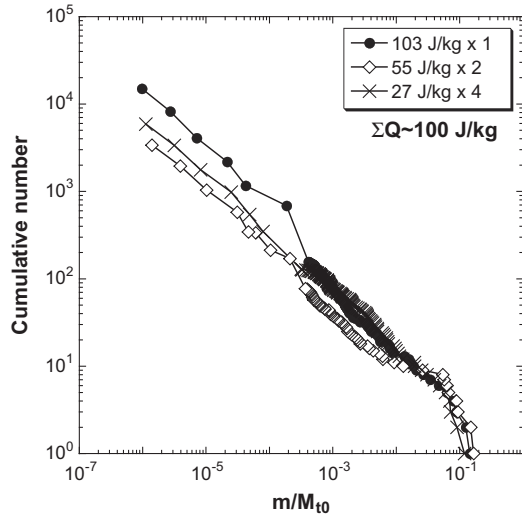


**Fig. 5.** Cumulative number of recovered impact fragments for the same targets as those shown in Fig. 4. The number in the  $\text{J kg}^{-1}$  before the “ $\times$ ” in the legend indicates the impact energy at each shot, and the number after the “ $\times$ ” in the legend indicates the number of impacts.

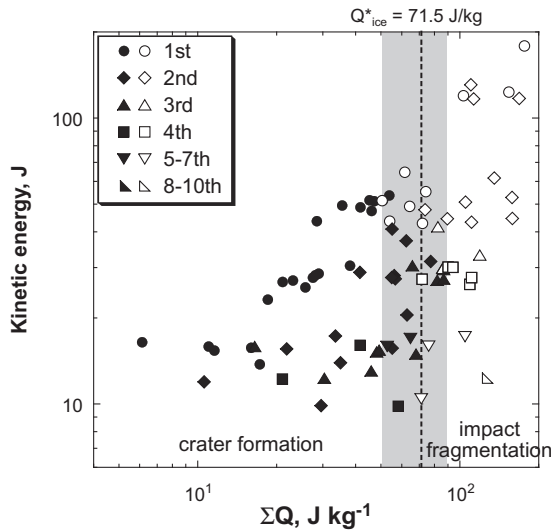


**Fig. 6.** The relationship between the kinetic energy of the projectile and the total energy density  $\Sigma Q$  with different number of impacts. The solid symbols show the largest impact fragment mass normalized by the initial target mass,  $m_i/M_{t0}$ , larger than 0.95 (crater formation), and the open symbols show those smaller than 0.95 (impact fragmentation). The dotted line shows the impact strength of polycrystalline ice for the single-impact experiments at the energy density smaller than  $400 \text{ J kg}^{-1}$  obtained by Kato et al. (1995). The gray zone shows the boundary area between the crater formation and the impact fragmentation.

From the results shown in Figs. 7 and 9, we found that the relationship between the normalized impact fragment mass  $m_i/M_{t0}$  and the single energy density  $Q_j$  depended on the number of impacts, whereas the relationship between  $m_i/M_{t0}$  and the total energy density  $\Sigma Q$  did not depend on the number of impacts. We speculate that the damage generated at every shot accumulates in the interior of the same target, which could explain our findings. However, further studies to clarify the elementary processes in pre-impacted targets are necessary to address this issue.

### 3.3.2. The size distributions of impact fragments

As explained in Section 3.3.1, the relationship between  $m_i/M_{t0}$  and  $\Sigma Q$  obtained by multiple impacts is similar to the relationship

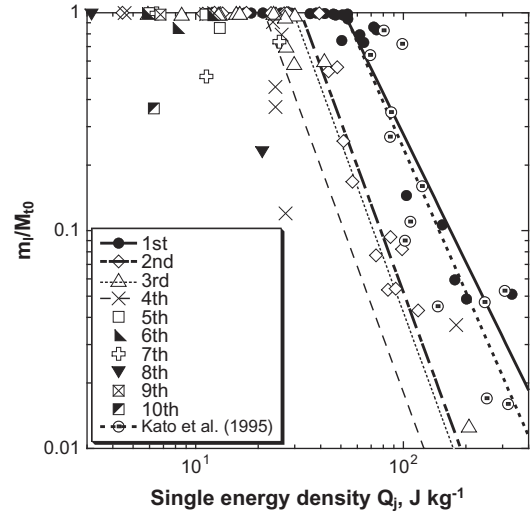


**Fig. 7.** The relationship between the largest fragment mass normalized by the initial target mass,  $m_i/M_{t0}$ , and the single energy density at the  $j$ th impact,  $Q_j$ .

**Table 2**

Parameters  $A$  and  $p$  of Eq. (2), and the impact strength  $Q^*$ .

	$A \text{ [J kg}^{-1} \text{]}^p$		Impact strength $Q^* \text{ (J kg}^{-1} \text{)}$
Number of impacts $j$ (our study)			
1	3.34 (0.45)	1.95 (0.22)	74.0
2	3.93 (0.65)	2.60 (0.35)	42.1
3	3.83 (0.14)	2.60 (assumed)	38.7
4	3.46 (0.23)	2.60 (assumed)	28.0
Kato et al. (1995) ( $j = 1$ )	3.76 (0.79)	2.19 (0.37)	71.5

The numbers in parentheses indicate the error.

obtained by a single impact, irrespective of the number of impacts. However, the size distribution of impact fragments in a fine range is quite different with the number of impacts even if the  $\Sigma Q$  is almost the same, as shown in Fig. 5. We therefore examined how the cumulative number of fine impact fragments depends on  $Q_j$  or  $\Sigma Q$ . To study the amount of fine fragments, we compared the number of fine fragments at  $m_i/M_{t0} \sim 10^{-6}$ ,  $n_m$ , which corresponds to the smallest fragment that we measured in this study. Fig. 10a and b shows the  $n_m$  as a function of total energy density  $\Sigma Q$  and single energy density  $Q_j$ , respectively. We chose these distributions for the  $m_i/M_{t0}$  smaller than 0.95, the group of impact fragmentation described in Section 3.3.1 and shown in Fig. 6. The data in Fig. 10a show that the  $n_m$  increases with the decrease of number of impacts. Notably, the  $n_m$  for the single impact was an order of magnitude larger than that for the seven-times impact and the ten-times impact at the same total energy densities,  $\sim 100 \text{ J kg}^{-1}$  and  $\sim 55 \text{ J kg}^{-1}$ . On the other hand, the  $n_m$  shown in Fig. 10b has a good correlation with  $Q_j$ , and it increased with the increase of  $Q_j$  even when the number of impacts was different. This means that the number of smallest fragments was determined by the single energy density  $Q_j$  rather than  $\Sigma Q$ . The relationship between  $n_m$  and  $Q_j$  could be fitted by a power law equation and is described by the following equation:

$$n_m = 10^{1.02 \pm 0.22} \cdot Q_j^{1.31 \pm 0.12}. \quad (4)$$

The cumulative number of impact fragments with the mass larger than  $m$ ,  $N(>m)$ , is described by the following equation (Takagi et al., 1984):

$$N(>m) = B \cdot (m/M_{t0})^{-q}, \quad (5)$$

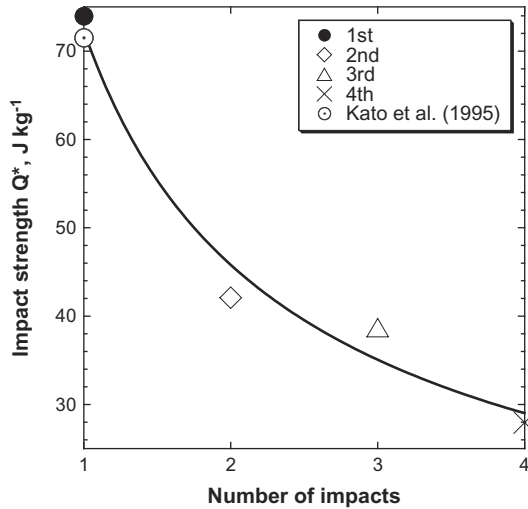


**Fig. 8.** The relationship between the impact strength,  $Q^*$ , and the number of impacts.

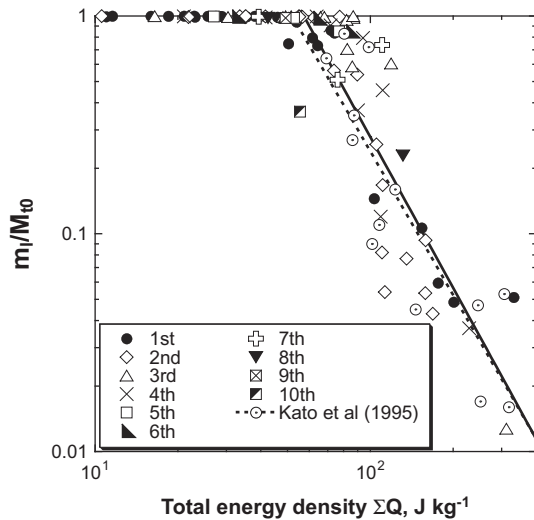


**Fig. 9.** The relationship between the largest fragment mass normalized by the initial target mass,  $m_l/M_0$ , and the total energy density from the first to the  $j$ th impact,  $\Sigma Q$ . The open circles represent the results of polycrystalline ice in the single-impact experiments at the energy density smaller than  $400 \text{ J kg}^{-1}$  conducted by Kato et al. (1995). The solid line represents the fitting line determined using the power law function of Eq. (3) at the normalized largest fragment mass smaller than 0.95.

where  $B$  and  $q$  are constants. The size distribution written by the cumulative numbers of fragments are believed to be divisible into three regimes according to the size of impact fragments. Regime 1 covers the size range of fragment mass normalized by the target mass from  $10^{-2}$  to  $10^{-3}$ . Regime 3 covers that from  $10^{-3}$  to  $10^{-5}$ , and regime 2 is the intermediate regime (Takagi et al., 1984), and thus the constants  $B$  and  $q$  are expected to change in each regime. We examined the  $B$  and  $q$  for all regimes in the normalized fragment mass larger than  $10^{-2}$  in regime 1, in that smaller than  $10^{-4}$  in regime 3, and in that between  $10^{-2}$  and  $10^{-4}$  in regime 2.

The  $B$  for each regime is as follows: from  $7.19 \times 10^{-3}$  to 1.19 in regime 1, from  $4.30 \times 10^{-3}$  to 2.50 in regime 2, and from  $7.24 \times 10^{-3}$  to 28.81 in regime 3. In regime 1, the  $B$  increased with the decrease of the number of impacts at the constant single energy density  $Q_j$ . This means that the normalized largest fragment mass  $m_l/M_0$  is larger as the number of impacts is smaller, and this

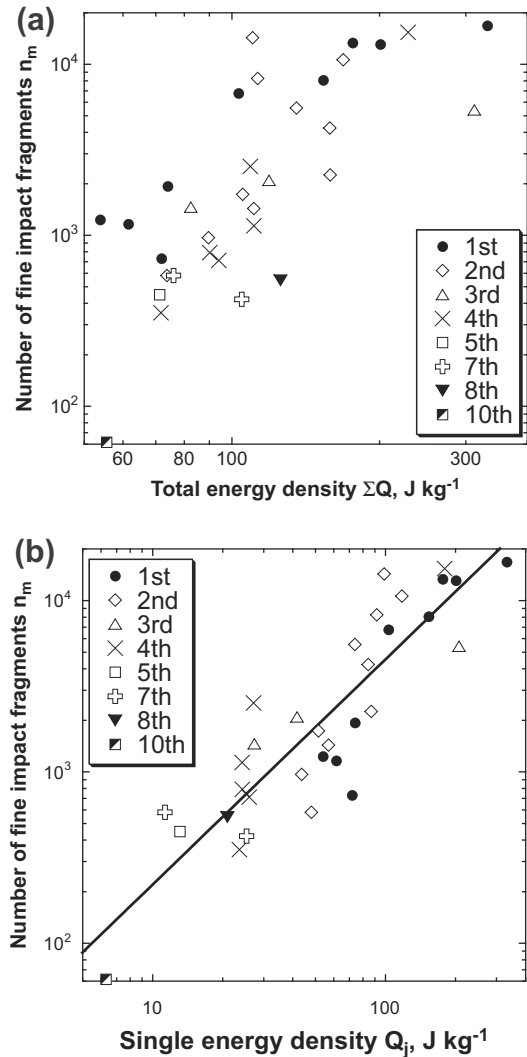


**Fig. 10.** The relationship between the number of fine impact fragments and (a) the total energy density,  $\Sigma Q$ , or (b) the single energy density,  $Q_j$ , respectively. The solid line in panel (b) represents the fitting line determined using the power law function of Eq. (4).

result is consistent with the results shown in Fig. 7. Similar results, in which  $B$  increased with the decrease of the number of impacts were observed in the other regimes.

The power law index  $q$  was 0.16–1.81 in regime 1 and 0.28–1.26 in regime 2. The  $q$  is independent on the number of impacts. In regime 2, the  $q$  increased with the decrease of the  $Q_j$ , whereas in regime 1 it was also independent on the  $Q_j$  within the error range. Several research groups have studied the  $q$  for regime 3 in impact experiments. Our  $q$  for regime 3 was found to be  $0.66 \pm 0.19$ . This value is close to that of polycrystalline cubic ices impacted by a nylon projectile with impact velocities from 2.3 to  $4.7 \text{ km s}^{-1}$  in single-impact experiments conducted by Arakawa (1999),  $0.64 \pm 0.06$ , whereas it is larger than that of rectangular parallelepiped ices impacted by a stainless steel ball with impact velocities up to  $5 \text{ km s}^{-1}$  in experiments performed by Miljkovic et al. (2011),  $0.49 \pm 0.05$ .

#### 4. Discussion

We would like to estimate the cumulative damage in small icy satellites generated by past impacts using the crater size

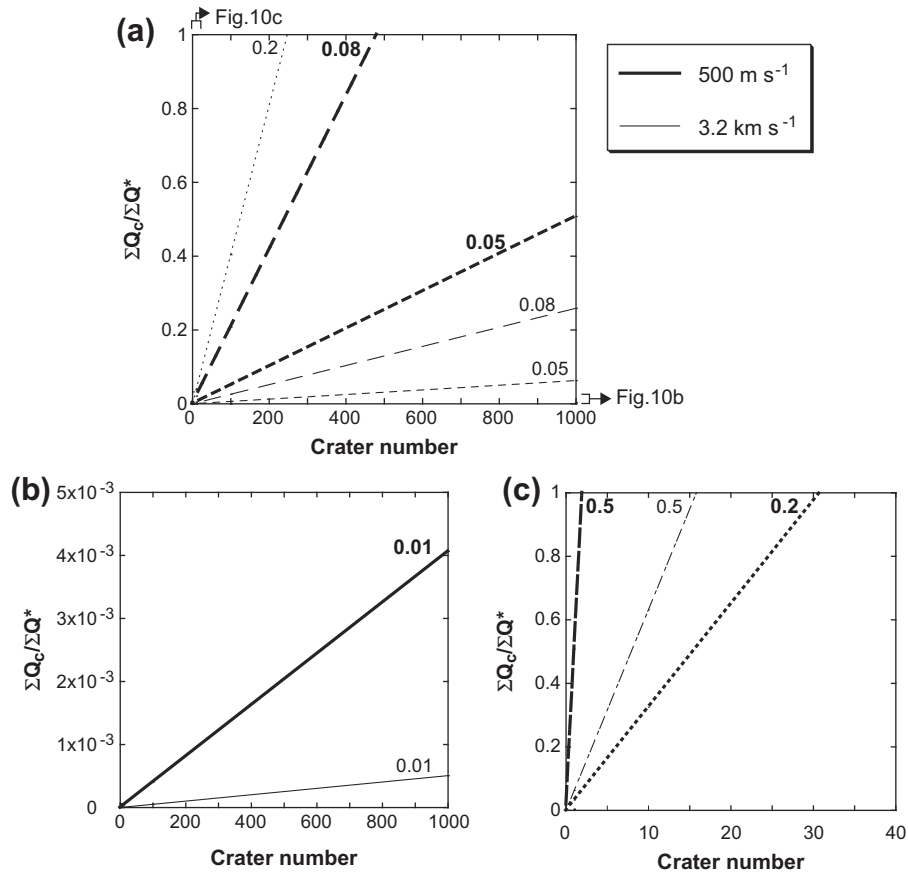


**Fig. 11.** The relationship between the cumulative damage of a theoretical icy body normalized by the impact strength of polycrystalline ice in the present multiple-impact experiments obtained in this study,  $\Sigma Q_c/\Sigma Q^*$ , and the crater number. Each line shows the difference of the ratio of the crater diameter to the target body diameter,  $D_{cr}/D_t$ , and the number near each line shows the value of  $D_{cr}/D_t$ . The thick line shows the results calculated at the impact speed of the impactor,  $500 \text{ m s}^{-1}$ , and the thin line shows that at  $3.2 \text{ km s}^{-1}$ . The enlarged part of the vertical axis ranging from 0 to  $5 \times 10^{-3}$  and the horizontal axis ranging from 0 to 40 are presented as panels (b) and (c), respectively.

distributions of actual small icy satellites, and here we discuss the degree of internal damage by comparing the estimated values with the impact strength. In this model, we calculate the energy density  $Q_c$  necessary for the formation of a crater having a certain diameter, and we estimate the total energy density  $\Sigma Q_c$  by accumulating the calculated energy densities  $Q_c$  from the crater sizes on these satellites. In order to estimate the individual  $Q_c$  corresponding to the crater, we must determine the impactor size and the impact velocity. In this discussion, we simply assume the crater formation mechanism in the strength regime because the small icy satellites have gravity that is rather weaker than that of the Earth, as weak as  $<10^{-3} \text{ G}$ . We then estimate the impactor size by using the cratering scaling law in the strength regime proposed by Housen et al. (1983).

The cratering scaling law used in this calculation is as follows:

$$\frac{R_{cr}}{r_p} = K \left( \frac{Y}{\rho_t V_i^2} \right)^\alpha, \quad (6)$$

where  $R_{cr}$  is the crater radius,  $r_p$  is the impactor radius,  $\rho_t$  is the density of the target body,  $V_i$  is the impact velocity,  $Y$  is the material strength, and  $K$  and  $\alpha$  are the constants, depending on the material properties. The non-dimensional parameters of  $R_{cr}/r_p$  and  $Y/\rho_t V_i^2$  can be expressed as  $\pi_R$  and  $\pi_Y$ , respectively, where we assume that the impactor and the target are the same materials in this model. We also assume the simple case that an impactor and a target body consist of polycrystalline ice without any inclusions, although it is well known that the mean densities of small icy satellites range from  $300$  to  $2600 \text{ kg m}^{-3}$ , and they are thought to be a mixture of

ice that includes non-water ice such as  $\text{CO}_2$ , rocky materials, and pores. Therefore, we ignore the density ratio of an impactor to a target body in Eq. (6) of this model, so that we use the crater scaling law of Eq. (6) for ice–ice impacts obtained by Iijima et al. (1995), written as  $\pi_R = 1.90\pi_Y^{-0.52}$ . We used the dynamical tensile strength of ice,  $17 \text{ MPa}$ , obtained by Stewart and Ahrens (1999), as the material strength,  $Y$ . We chose the impact velocities of  $V_i$ ,  $500 \text{ m s}^{-1}$ , which corresponds to a probable collisional speed of the Kuiper belt objects estimated by the numerical simulation for collisions with minor bodies in the Kuiper belt by Dell'Oro et al. (2001), and  $3.2 \text{ km s}^{-1}$ , which corresponds to a typical collisional speed of present outer icy satellites such as Phoebe orbiting Saturn, estimated by using the numerical simulations of collisions of icy satellites with comets in the outer Solar System by Zahnle et al. (2003).

First, we calculate the  $Q_c$  of hypothetical icy satellites with craters with a single crater size. That is, the  $\Sigma Q_c$  is described as  $\Sigma Q_c = nQ_c$ , where  $n$  is the crater number. In this calculation, the crater diameter normalized by the target diameter,  $D_{cr}/D_t$ , was changed from  $0.01$  to  $0.5$ .

Fig. 11 shows the relationship between the crater number and the cumulative damage  $\Sigma Q_c$  normalized by the impact strength  $\Sigma Q^*$  obtained by this impact experiment,  $77.6 \text{ J kg}^{-1}$ , so that the unity of  $\Sigma Q_c/\Sigma Q^*$  means that the target body would disrupt catastrophically. At the constant impact velocity, the cumulative damage  $\Sigma Q_c$  increases with the increase of the ratio of the crater diameter to the target body diameter. For example, in the case of  $V_i = 500 \text{ m s}^{-1}$ , the  $\Sigma Q_c$  is almost zero at the diameter ratio of  $0.01$ ; that is, the target body is hardly damaged, whereas at the diameter ratio of  $0.5$ , the  $\Sigma Q_c$  increases abruptly and then the

target body disrupts catastrophically after the two impacts of the small body.

At the constant diameter ratio, the  $\Sigma Q_c$  decreases with the increase of the impact velocity; the number of colliding small bodies necessary for the catastrophic disruption of the target body ( $\Sigma Q_c/\Sigma Q^* = 1$ ) at  $V_i = 3.2 \text{ km s}^{-1}$  is about eight times larger than that at  $V_i = 500 \text{ m s}^{-1}$ . In the same manner, we were able to easily calculate the cumulative damage of actual small bodies by using their crater size distributions on the surface.

Lastly, we estimate the cumulative damage of a saturnian icy satellite, Phoebe, by using the method described above. The mean density,  $\rho_i$ , is  $1630 \text{ kg m}^{-3}$  (Porco et al., 2005). As the impact velocity,  $V_i$ , we chose to be  $500 \text{ m s}^{-1}$  and  $3.2 \text{ km s}^{-1}$ . We used the database of impact craters of Phoebe provided by the WGPSN (Working Group for Planetary System Nomenclature) at IAU for the crater diameters larger than 10 km, and we used the cumulative crater size distribution obtained by Kirchoff and Schenk (2009a,b) for the crater diameters smaller than 10 km.

The cumulative damage in the target body can be calculated by using Eq. (6), the scaling parameters obtained by Iijima et al. (1995), and the crater size distribution as follows:

$$\Sigma Q_c = \frac{(3.07 \times 10^{-1}) \rho_p Y^{1.56}}{M_t \rho_i^{1.56} V_i^{1.12}} \Sigma (R_{cr}^3), \quad (7)$$

where  $\rho_p$  is the density of the impactor (in this case,  $\rho_p = 917 \text{ kg m}^{-3}$ ) and  $M_t$  is the mass of the target body (in this case, the mass of Phoebe). As a result, the cumulative damage for Phoebe is  $22.1 \text{ J kg}^{-1}$  or  $6.72 \times 10^{-2} \text{ J kg}^{-1}$  at the impact velocity of  $500 \text{ m s}^{-1}$  or  $3.2 \text{ km s}^{-1}$ , respectively, by using only the data for the crater diameters  $>10 \text{ km}$ . Even if we consider the data for the crater diameters  $<10 \text{ km}$ , this damage is not changed much:  $22.3 \text{ J kg}^{-1}$  and  $6.78 \times 10^{-2} \text{ J kg}^{-1}$ . Phoebe also has a crater with a diameter larger than 100 km, Jason crater. We found that the energy density necessary for the formation of this crater was one-third of the total energy density,  $\Sigma Q_c$ .

We know that the impact strength of polycrystalline ice for multiple impacts  $\Sigma Q^*$  is  $77.6 \text{ J kg}^{-1}$ , irrespective of the number of impacts, so we can say that the cumulative damage in Phoebe is as large as approx. 30% of the intact body if the impact speed of the impactor is  $500 \text{ m s}^{-1}$ . On the other hand, the cumulative damage is almost zero if the impact speed of the impactor is  $3.2 \text{ km s}^{-1}$ . Thus, we notice that the cumulative damage is significantly dependent on the impact speed of the impactor. However, the generated fractures in the target body have been sintered after the formation of these craters by the impact, although the sintering duration might be very long to heal these fractures.

From these results, we speculate that the interior of Phoebe is as follows. In the case of the impacts at  $3.2 \text{ km s}^{-1}$ , the impact energy necessary to form each crater on Phoebe is much smaller than the  $\Sigma Q^*$ , and thus we suspect that the impactors excavated just under the impact surface, and the re-accumulated ejecta layer, the so-called “regolith layer”, was formed on the surface of Phoebe. On the other hand, in the case of impacts at  $500 \text{ m s}^{-1}$ , the energy necessary to form some larger craters is larger ( $>1 \text{ J kg}^{-1}$ ) than that at  $3.2 \text{ km s}^{-1}$ , and thus some large cracks might exist under these craters. However, the energies necessary to form other craters are not so large, and thus the regolith was also formed on the surface, as in the case of the impacts at  $3.2 \text{ km s}^{-1}$ .

It has been speculated that the crater formation occurs in the gravity regime on middle-to-large icy satellites, at the radius of a few tens of km, depending on the model (e.g., Benz and Asphang, 1999; Stewart and Leinhardt, 2009). Thus, we calculated the  $\Sigma Q_c$  of Phoebe based on the scaling law of the gravity regime. However, there are no experimental data for ice–ice impacts in the gravity regime, so we used the cratering scaling law of dry sand in the

gravity regime summarized in Housen and Holsapple (2011). As a result, the  $\Sigma Q_c$  is more than  $2500 \text{ J kg}^{-1}$  at both impactor speeds, and thus the catastrophic disruption should occur, and this is not realistic. It is advisable to revise the crater scaling laws in the gravity regime suitable for Phoebe. We plan to study the crater scaling law in the gravity regime for porous ice–silicate mixtures (which are applicable to Phoebe) in the future.

## 5. Summary

We conducted multiple-impact experiments for polycrystalline ice targets at impact velocities from  $84$  to  $502 \text{ m s}^{-1}$  and using the number of impacts from 1 to 10 times, and we studied the effects of multiple impacts on the impact strength, the size distribution of impact fragments, and the ejecta velocity. Our results are summarized as follows:

1. The fragment velocities at two corners on the impact surface in the center of the mass system,  $V_{e-g}$ , had a good correlation with the single energy density  $Q_j$ , and they increased with the increase of  $Q_j$  irrespective of the number of impacts for each target. The relationship between the  $V_{e-g}$  and the  $Q_j$  was obtained as  $V_{e-g} = 10^{-1.53 \pm 0.18} \cdot Q_j^{1.03 \pm 0.09}$ .
2. The onset of impact fragmentation and the largest fragment mass could be described by the total energy density,  $\Sigma Q$ . The onset of impact fragmentation for the pre-impacted ice,  $\Sigma Q_{\text{onset}}$ , was  $68.6 \pm 18.2 \text{ J kg}^{-1}$ . The impact strength  $\Sigma Q^*$ , which was defined as the  $\Sigma Q$  when the  $m_i/M_{t0}$  was one-half of the initial target mass, was  $77.6 \text{ J kg}^{-1}$ , which is very close to be the impact strength of polycrystalline ice in single-impact experiments conducted by Kato et al. (1995).
3. The number of fine fragments at  $m/M_{t0} \sim 10^{-6}$ ,  $n_m$ , was well correlated with the single energy density  $Q_j$ , and the relationship was written as  $n_m = 10^{1.02 \pm 0.22} \cdot Q_j^{1.31 \pm 0.12}$ . The cumulative number of impact fragments  $N(>m)$  was described as  $N(>m) = B \cdot (m/M_{t0})^{-q}$ , and the power law index  $q$ , in the normalized fragment mass smaller than  $10^{-4}$ , was obtained as  $0.66 \pm 0.19$ . This value is close to that of polycrystalline ice in the single-impact experiments performed by Arakawa (1999).
4. We estimated the internal cumulative damage of small icy satellites caused by past impacts according to the crater scaling law proposed by Housen et al. (1983) and the cumulative size distributions of impact craters on these satellites. In the case of hypothetical icy bodies with constant-size craters on these surfaces, the cumulative damage  $\Sigma Q_c$  increases with the increase of the ratio of the crater diameter to the target body diameter and decreased with the increase of the impact velocity of the impactor. We estimated the  $\Sigma Q_c$  for the saturnian satellite Phoebe by using the database of impact craters provided by WGPSN at IAU and the cumulative crater size distribution obtained by Kirchoff and Schenk (2009a,b), and we observed the  $\Sigma Q_c$  of  $22.3 \text{ J kg}^{-1}$  at the impact velocity  $500 \text{ m s}^{-1}$ , which was about one-third of the impact strength  $\Sigma Q^*$ , and  $6.78 \times 10^{-2} \text{ J kg}^{-1}$  at impact velocity  $3.2 \text{ km s}^{-1}$ , which was close to zero, so that the damage was hardly accumulated in the interior of the target body.

## Acknowledgments

We thank Mr. S. Nakatsubo of the Contribution Division of the Institute of Low Temperature Science, Hokkaido University, for his technical help. We also appreciate the help with the experiments provided by Dr. Yuri Shimaki of the Institute for the Study of the Earth's Interior, Okayama University. This work was

supported in part by Grants-in-Aid for Scientific Research (22244056, 23103004, and 25870419) from the Japan Ministry of Education, Culture, Sports, Science and Technology, and by a grant for a Joint Research Program from the Institute of Low Temperature Science, Hokkaido University.

## Appendix A. Supplementary material

Supplementary data associated with this article can be found, in the online version, at <http://dx.doi.org/10.1016/j.icarus.2014.02.008>.

## References

- Arakawa, M., 1999. Collisional disruption of ice by high-velocity impact. *Icarus* 142, 34–45.
- Arakawa, M., Tomizuka, D., 2004. Ice–silicate fractionation among icy bodies due to the difference of impact strength between ice and ice–silicate mixture. *Icarus* 170, 193–201.
- Arakawa, M., Leliwa-Kopystynski, J., Maeno, N., 2002. Impact experiments on porous icy–silicate cylindrical blocks and the implication for disruption and accumulation of small icy bodies. *Icarus* 158, 516–531.
- Benz, W., Asphang, E., 1999. Catastrophic disruption revisited. *Icarus* 142, 5–20.
- Benz, W., Asphaug, E., 1993. Impact simulations with fracture. I. Method and tests. *Icarus* 107, 98–116.
- Britt, D.T., Yeoman, D., Housen, K., Consolmagno, G., 2002. Asteroid density, porosity, and structure. In: Bottke, W.F., Cellino, A., Paolicchi, P., Binzel, R. (Eds.), *Asteroids III*. Univ. Arizona Press, Tucson, AZ, pp. 485–500.
- Consolmagno, G.J., Britt, D.T., 1998. The density and porosity of meteorites from the Vatican collection. *Meteorit. Planet. Sci.* 33, 1231–1240.
- Davis, D.R., Ryan, E.V., 1990. On collisional disruption: Experimental results and scaling law. *Icarus* 83, 156–182.
- Dell'Oro, A., Marzari, F., Paolicchi, P., Vanzani, V., 2001. Updated collisional probabilities of minor body populations. *Astron. Astrophys.* 366, 1053–1060.
- Fujiwara, A., Tsukamoto, A., 1980. Experimental study on the velocity of fragments in collisional breakup. *Icarus* 44, 142–153.
- Fujiwara, A., Kamimoto, G., Tsukamoto, A., 1977. Destruction of basaltic bodies by high-velocity impact. *Icarus* 31, 277–288.
- Gault, D.E., Wedekind, J.A., 1969. The destruction of tektites by micrometeoroid impact. *J. Geophys. Res.* 74, 6780–6794.
- Housen, K., 2009. Cumulative damage in strength-dominated collisions of rocky asteroids: Rubble piles and brick piles. *Planet. Space Sci.* 57, 142–153.
- Housen, K., Holsapple, K.A., 2011. Ejecta from impact craters. *Icarus* 211, 856–875.
- Housen, K.R., Schmidt, R.M., Holsapple, K.A., 1983. Crater ejecta scaling laws: Fundamental forms based on dimensional analysis. *J. Geophys. Res.* 88, 2485–2499.
- Iijima, Y., Kato, M., Arakawa, M., Maeno, N., Fujiwara, A., Mizutani, H., 1995. Cratering experiments on ice: Dependence of crater formation on projectile materials and scaling parameter. *Geophys. Res. Lett.* 22, 2005–2008.
- Kato, M. et al., 1992. Impact experiments on low temperature H<sub>2</sub>O ice. In: Maeno, N., Hondoh, T. (Eds.), *Physics and Chemistry of Ice*. Hokkaido Univ. Press, Japan, pp. 237–244.
- Kato, M., Iijima, Y., Arakawa, M., Okimura, Y., Fujiwara, A., Maeno, N., Mizutani, H., 1995. Ice-on-ice impact experiments. *Icarus* 113, 423–441.
- Kawakami, S., Mizutani, H., Takagi, Y., Kato, M., Kumazawa, M., 1983. Impact experiments on ice. *J. Geophys. Res.* 88, 5806–5814.
- Kirchoff, M.R., Schenk, P., 2009a. Crater modification and geologic activity in Enceladus' heavily cratered plains: Evidence from the impact crater distribution. *Icarus* 202, 656–668.
- Kirchoff, M.R., Schenk, P., 2009b. Impact cratering records of the mid-sized, icy saturnian satellites. *Icarus* 206, 485–497.
- Michel, P., Benz, W., Richardson, D.C., 2003. Disruption of fragmented parent bodies as the origin of asteroid families. *Nature* 421, 608–611.
- Miljkovic, K., Mason, N.J., Zarnecki, J.C., 2011. Ejecta fragmentation in impacts into gypsum and water ice. *Icarus* 214, 739–747.
- Nakamura, A.M., Fujiwara, A., Kadono, T., Shirono, S., 1994. Fragmentation of intact and pre-impacted basalt target. In: Kozai, Y., Binzel, R.P., Hirayama T. (Eds.), *Seventy-Five Years of Hirayama Asteroid Families*, ASP Conference Series 63, pp. 237–242.
- Porco, C.C. et al., 2005. Cassini imaging science: Initial results on Phoebe and Iapetus. *Science* 307, 1237–1242.
- Porco, C.C., Thomas, P.C., Weiss, J.W., Richardson, D.C., 2007. Saturn's small inner satellites: Clues to their origins. *Science* 318, 1602–1607.
- Shimaki, Y., Arakawa, M., 2012. Experimental study on collisional disruption of highly porous icy bodies. *Icarus* 218, 737–750.
- Stewart, S.T., Ahrens, T.J., 1999. Correction to the dynamic tensile strength of ice and ice–silicate mixtures (Lange & Ahrens 1983). *Lunar Planet. Sci.* 30, 2037.
- Stewart, S.T., Leinhardt, Z.M., 2009. Velocity-dependent catastrophic disruption criteria for planetesimals. *Astrophys. J.* 691, L133–L137.
- Takagi, Y., Mizutani, H., Kawakami, S., 1984. Impact fragmentation experiments of basalts and pyrophyllites. *Icarus* 59, 462–477.
- Veverka, J. et al., 2000. NEAR at Eros: Imaging and spectral results. *Science* 289, 2088–2097.
- Yasui, M., Arakawa, M., 2011. Impact experiments of porous gypsum–glass bead mixtures simulating parent bodies of ordinary chondrites: Implications for re-accumulation processes related to rubble–pile formation. *Icarus* 214, 754–765.
- Yasui, M., Arakawa, M., Hasegawa, S., Fujita, Y., Kadono, T., 2012. In situ flash X-ray observation of projectile penetration processes and crater cavity growth in porous gypsum target analogous to low-density asteroids. *Icarus* 221, 646–657.
- Zahnle, K., Schenk, P., Levison, H., Dones, L., 2003. Cratering rates in the outer Solar System. *Icarus* 163, 263–289.